


On the distributions of fuel droplets and *in situ* vapor in rotating detonation combustion with prevaporized *n*-heptane sprays

Cite as: Phys. Fluids **33**, 043307 (2021); <https://doi.org/10.1063/5.0045222>

Submitted: 24 January 2021 . Accepted: 19 March 2021 . Published Online: 07 April 2021

Qingyang Meng (孟庆洋), Ningbo Zhao (赵宁波), and  Huangwei Zhang (张黄伟)



View Online



Export Citation



CrossMark

Physics of Fluids

SPECIAL TOPIC: Tribute to
Frank M. White on his 88th Anniversary

SUBMIT TODAY!

On the distributions of fuel droplets and *in situ* vapor in rotating detonation combustion with prevaporized *n*-heptane sprays

Cite as: Phys. Fluids **33**, 043307 (2021); doi: 10.1063/5.0045222

Submitted: 24 January 2021 · Accepted: 19 March 2021 ·

Published Online: 7 April 2021




View Online



Export Citation



CrossMark

Qingyang Meng (孟庆洋),^{1,2} Ningbo Zhao (赵宁波),¹ and Huangwei Zhang (张黄伟)^{2,a)} 

AFFILIATIONS

¹College of Power and Energy Engineering, Harbin Engineering University, Harbin 150001, China

²Department of Mechanical Engineering, National University of Singapore, 9 Engineering Drive 1, Singapore 117576, Republic of Singapore

^{a)}Author to whom correspondence should be addressed: huangwei.zhang@nus.edu.sg. Tel.: +65 6516 2557. Fax: +65 6779 1459

ABSTRACT

Rotating detonation combustion fueled with partially prevaporized *n*-heptane sprays is studied with the Eulerian–Lagrangian method. A flattened two-dimensional domain with periodic boundaries is considered to mimic the annular rotating detonation combustor. This work focuses on the effects of prevaporized gas temperature and equivalence ratio on two-phase rotating detonation wave propagation and *n*-heptane droplet vaporization characteristics in the refill zone. The results show that gas temperature has a great impact on *n*-heptane sprays vaporization in the refill zone. The droplet evaporation rate increases with the gas temperature, especially when they are close to the deflagration surface. High evaporation rate can be observed for those droplets that are freshly injected into the chamber because they closely interact with the hot product gas from the previous cycle of the rotating detonation. A vapor layer between the droplet-laden area and deflagration surface exists and high concentrations of *n*-heptane can be found along the deflagration surface. A conceptual model for the droplet and vapor distribution in the refill zone is proposed. The results also show that the blast waves can encroach the refill zone and therefore influence the droplet thermodynamic properties inside the refill zone. The blast waves influence the droplet evaporation rate but have limited effects on droplet temperature, diameter, and spatial distributions. Also, the detonation propagation speed increases with increased prevaporized gas temperature and/or equivalence ratio. The detonation cell size decreases and becomes more uniform as the reactant temperature increases. Moreover, the size and irregularity of rotating detonation cells increase when the prevaporized gas equivalence ratio decreases.

Published under license by AIP Publishing. <https://doi.org/10.1063/5.0045222>

I. INTRODUCTION

Detonation engine is one of the most promising propulsive devices due to the high thermodynamic cycle efficiency and pressure-gain performance.^{1,2} Typical detonation engines can be classified by their individual operational features, such as rotating detonation engine (RDE),^{3,4} pulsed detonation engine (PDE),^{5,6} and oblique detonation engine (ODE).^{7,8} As one of the realizable and scalable detonation engines, RDE confines the detonation wave within a narrow annular channel, where the propellant is continuously injected from the inlet and detonation product exits from the outlet to generate the thrust.^{9–13} Continuous propagation of detonation waves makes RDE produce stable propulsive output and also simplifies the ignition implementations. Considering the limited storage space in practical propulsion systems, e.g., rocket engines, propellants with high energy density are desirable and utilization of liquid fuels is a key step for RDE commercialization.

Liquid-fuel RDE experiments have been conducted in 1960s–1970s for the development of rocket-type propulsion technologies.¹⁴ Recently, interests in liquid-fuel RDE are resparked and several ground tests have been successfully conducted. For instance, Bykovskii *et al.* used liquid kerosene in their RDE experiments.^{15–17} They first chose a small combustor with a diameter being 306 mm and selected oxygen-enriched air as the oxidant to achieve a stable rotating detonation wave (RDW). In their recent experiments, hydrogen or syngas is used and the diameter of the RDE combustor is increased to 503 mm.^{17,18} Their results show that the RDW cannot be achieved without additives (i.e., hydrogen or syngas) when standard air is used as the oxidant.

Kindracki¹⁹ studied kerosene atomization quality in different gas velocities and kerosene injection patterns by injecting liquid kerosene into cold nitrogen stream. Their results show that the diameters of the

sprayed kerosene droplets range from 20 to 40 μm . He also investigated the initiation and propagation characteristics of RDW with liquid kerosene and air and successfully achieved the self-sustained detonation wave using liquid kerosene and air mixture with the addition of hydrogen.²⁰

The foregoing experimental investigations have demonstrated the feasibility of rotating detonation combustion with liquid fuel sprays, but one may need to resort to high-fidelity numerical simulations to gain deeper scientific insight into two-phase RDEs, such as droplet vaporization and movement in the RDE chamber, as well as fuel vapor distributions. There have already been some computational efforts. For example, Sun and Ma²¹ investigated the effect of air total temperature and octane injection width on RDW propagation. They pointed out that the detonation wave speed decreases with increased octane injection width. They also found that there was a critical fuel injection width for a fixed air temperature. Moreover, Hayashi *et al.*²² numerically studied the RDW behaviors under different droplet sizes and prevaporization degrees using JP-10/air as the reactant. They found that the unburned fuel pockets exist in postshock region and the interactions between the fuel droplets and detonation wave may cause the RDW extinction. However, since Eulerian–Eulerian method is used in their work, the individual behaviors of liquid fuel droplets cannot be captured.

We numerically studied partially prevaporized *n*-heptane sprays with Eulerian–Lagrangian method and analyzed the effects of droplet sizes on the RDW behaviors.²³ It is found that the RDW propagation speed is jointly affected by droplet size and gaseous premixture equivalence ratio. Furthermore, the detonated fuel fraction first decreases, reaches the minimum values when the droplet diameter is around 20 μm , and then increases when the diameter increases toward 50 μm . This indicates the strong correlation between the droplet sizes and liquid fuel detonative combustion efficiency. Nevertheless, the interactions of the droplets and gas phase inside the fuel refill zone and how their distributions affect the RDC are not discussed.²³

In this work, we will study the distributions of *n*-heptane droplets and vapor in the fuel refill zone of rotating detonation combustion, as well as their interactions with the key aerodynamic features and reactive flow structures (e.g., shock wave and deflagration surface). Hybrid Eulerian–Lagrangian method is used to simulate the compressible reactive flows laden with dispersed fuel droplets and two-way gas–liquid coupling is considered. A two-dimensional flatten domain is employed to mimic an annular RDE combustor. In particular, different from our previous studies,²³ the influences of preheated propellant properties (e.g., prevaporized gas temperature and equivalence ratio) on the RDW behaviors and droplet evaporation are studied, which is of great high relevance to practical implementations of RDEs with fuel sprays.^{15–17,20} The rest of the manuscript is organized as below. Governing equations and numerical methods are specified in Sec. II. Physical model and simulated operating conditions are introduced in Sec. III. Numerical results and discussions are presented in Sec. IV, with the main findings being summarized in Sec. V.

II. GOVERNING EQUATION AND NUMERICAL IMPLEMENTATION

A. Governing equation for gas phase

The gas phase is solved by the transport equations for compressible, two-phase, reacting flows with ideal gas equation of state. The

volume fraction effects of the dispersed phase on the gas phase properties are not considered, since dilute sprays are studied in this work.²⁴ The equations of mass, momentum, energy, and species mass fraction, respectively, read

$$\frac{\partial \rho}{\partial t} + \nabla \cdot [\rho \mathbf{u}] = S_{\text{mass}}, \quad (1)$$

$$\frac{\partial (\rho \mathbf{u})}{\partial t} + \nabla \cdot [\mathbf{u}(\rho \mathbf{u})] + \nabla p + \nabla \cdot \mathbf{T} = \mathbf{S}_{\text{mom}}, \quad (2)$$

$$\frac{\partial (\rho E)}{\partial t} + \nabla \cdot [\mathbf{u}(\rho E + p)] + \nabla \cdot [\mathbf{T} \cdot \mathbf{u}] + \nabla \cdot \mathbf{j} = \dot{\omega}_T + S_{\text{energy}}, \quad (3)$$

$$\frac{\partial (\rho Y_m)}{\partial t} + \nabla \cdot [\mathbf{u}(\rho Y_m)] + \nabla \cdot \mathbf{s}_m = \dot{\omega}_m + S_{\text{species},m}, \quad (m = 1, \dots, M-1), \quad (4)$$

$$p = \rho RT. \quad (5)$$

Here t is time, ρ is the density, \mathbf{u} is the velocity vector, T is the temperature, p is the pressure, Y_m is the mass fraction of m th species, M is the total species number, and E is the total energy. R in Eq. (5) is the specific gas constant. Only $(M-1)$ species equations are solved, and the inert species (such as nitrogen) can be calculated from $\sum_{m=1}^M Y_m = 1$. The source terms, S_{mass} , \mathbf{S}_{mom} , S_{energy} , and $S_{\text{species},m}$, denote the inter-phase exchange of mass, momentum, energy, and species, respectively, and given in Eqs. (13)–(16). \mathbf{T} is the viscous stress tensor, while \mathbf{j} is the diffusive heat flux and follows Fourier's law. Furthermore, \mathbf{s}_m is the species mass flux, $\dot{\omega}_m$ is the net production rate of m -th species, and $\dot{\omega}_T$ is the heat release from chemical reactions.

B. Governing equation for liquid phase

The liquid fuel sprays are modeled as a large number of spherical droplets. The droplet volume fraction is low (less than 1%), and therefore, the inter-droplet collision is neglected.²⁴ Also, the droplet breakup process is not considered due to the small diameter studied (i.e., 5 μm). The evolutions of mass, velocity, and temperature of individual fuel droplets are updated based on the Lagrangian method.²⁵ The corresponding equations, respectively, are

$$\frac{dm_d}{dt} = -\dot{m}_d, \quad (6)$$

$$\frac{d\mathbf{u}_d}{dt} = \frac{\mathbf{F}_d}{m_d}, \quad (7)$$

$$c_{p,d} \frac{dT_d}{dt} = \frac{\dot{Q}_c + \dot{Q}_{\text{lat}}}{m_d}. \quad (8)$$

Here m_d is the droplet mass, \mathbf{u}_d is the droplet velocity vector, and T_d is the droplet temperature. The droplet evaporation rate \dot{m}_d is calculated from

$$\dot{m}_d = \pi d_d Sh D_{ab} \rho_S \ln(1 + X_r), \quad (9)$$

where d_d is the droplet diameter, D_{ab} is the vapor diffusivity in the gaseous mixture, and ρ_S is the density on the droplet surface. $Sh = 2.0 + 0.6 Re_d^{1/2} Sc^{1/3}$ is the Sherwood number, and Sc is the Schmidt number of the gas phase. The droplet Reynolds number, Re_d , is defined based on the velocity difference between two phases, i.e., $Re_d \equiv \rho_d d_d |\mathbf{u}_{\text{gd}} - \mathbf{u}_d| / \mu$. Here ρ_d is the droplet material density, μ is the dynamic viscosity of the gaseous mixture, and \mathbf{u}_{gd} is the gas phase

velocity at the Lagrangian droplet location. In Eq. (9), $X_r = (X_S - X_C)/(1 - X_S)$ is the concentration difference between the ambient gas and droplet surface, scaled by that between the droplet surface and interior. Here X_C is the fuel species molar fraction in the surrounding gas, while X_S is the fuel species molar fraction at the droplet surface.

In Eq. (7), \mathbf{F}_d is the force acting on the droplet, including the Stokes drag force [I in Eq. (10)] and pressure gradient force (II)²⁴

$$\mathbf{F}_d = \underbrace{\frac{18\mu C_d Re_d}{\rho_d d_d^2} m_d (\mathbf{u}_{@d} - \mathbf{u}_d)}_I - \underbrace{\frac{1}{6} \pi d_d^3 \nabla p}_{II}. \quad (10)$$

Here C_d is the drag coefficient, and Re_d is the droplet Reynolds number, based on the slip velocity between gas and droplet phases.

The convective heat transfer rate \dot{Q}_c is calculated from

$$\dot{Q}_c = h_c A_d (T_{@d} - T_d), \quad (11)$$

where A_d is the surface area of a single droplet, h_c is the convective heat transfer coefficient, $T_{@d}$ is the gas temperature at the droplet location. Moreover, evaporation-induced heat transfer, \dot{Q}_{lat} , is estimated as

$$\dot{Q}_{lat} = h_{g,boil} - h_{l,boil}, \quad (12)$$

where $h_{g,boil}$ and $h_{l,boil}$ are, respectively, the enthalpies of carrier gas phase and liquid phase under the droplet boiling temperature.

The source terms in Eqs. (1)–(4) account for the effects of dispersed liquid fuel droplets on the gas phase and are calculated based on the properties of the droplets in individual CFD cells, i.e.,

$$S_{mass} = \frac{1}{V_c} \sum_1^{N_d} \dot{m}_d, \quad (13)$$

$$S_{mom} = -\frac{1}{V_c} \sum_1^{N_d} (-\dot{m}_d \mathbf{u}_d + \mathbf{F}_d), \quad (14)$$

$$S_{energy} = -\frac{1}{V_c} \sum_1^{N_d} (\dot{Q}_c - \dot{m}_d h_{g,boil}), \quad (15)$$

$$S_{species,m} = \begin{cases} S_{mass} & \text{for condensed species} \\ 0 & \text{for other species.} \end{cases} \quad (16)$$

Here V_c is the CFD cell volume and N_d is the droplet number in a cell. Note that $-\dot{m}_d \mathbf{u}_d$ in Eq. (14) represents the evaporation-induced momentum exchange between the gas and liquid phases. More detailed information about the gas phase and liquid phase equations and submodels used in Sec. II A and this section can be found in Refs. 23 and 26.

C. Computational implementation

The governing equations for gas and droplet phases are solved by a hybrid Eulerian–Lagrangian solver, *RYrhoCentralFoam*,²⁷ which is

developed based on a compressible flow solver *rhoCentralFoam* in OpenFOAM.²⁸ The accuracies of *RYrhoCentralFoam* have been confirmed through extensive benchmark tests, in terms of predicting shock waves, species diffusion, shock-chemistry interaction, detonation cell size, and frontal structure.^{26,29–31} Droplet models (e.g., evaporation) and two-phase interactions are also validated and verified, and it is shown that the *RYrhoCentralFoam* solver can accurately capture the individual droplet response to a flow with shock waves and chemical reactions.²⁶ The foregoing validation and verifications of *RYrhoCentralFoam* have been collectively shown in Ref. 27. Recently, this solver has been successfully used for modeling RDE with gaseous and liquid fuels.^{23,30,32}

The gas phase equations [i.e., Eqs. (1)–(4)] are discretized with cell-centred finite volume method. Second-order implicit backward scheme is applied for time discretization, and the time step is about 10^{-9} s (CFL number is around 0.1). Second-order Godunov-type upwind-central scheme developed by Kurganov *et al.*³³ is used for calculating the convection term in the momentum equation, while the TVD (total variation diminishing) scheme is used for the convection term in the energy and species mass fraction equations. Second-order central differencing scheme is applied for the diffusion terms in Eqs. (1)–(4).

The chemical terms in Eqs. (3) and (4), $\dot{\omega}_m$ and $\dot{\omega}_T$, are integrated with the Euler implicit method. Two-step reactions of *n*-C₇H₁₆ oxidation are employed in this work, which is listed in Table I with their respective parameters for Arrhenius kinetics.^{34,35} In Table I, A is the pre-exponential factor, n is the temperature exponent, E_a is the activation energy, a and b are the fuel and oxidizer reaction orders, respectively. It should be noted that to differentiate the *n*-heptane species from prevaporization and *in situ* droplet evaporation in the RDE chamber, we respectively use “*n*-C₇H₁₆” and “*n*-C₇H₁₆(v)” to denote them. Accordingly, they have separate reactions I and II, with identical kinetic parameters. The current reaction model is validated against a skeletal mechanism³⁶ through calculations of *n*-C₇H₁₆/air ZND (Zeldovich–von Newmann–Döring) structures with SD Toolbox³⁷ (see the Appendix A), and it is shown that it can correctly reproduce the detonation propagation speed, pressure, and temperature at both von Neumann and Chapman–Jouguet conditions in the ZND structures.

Moreover, the governing equations of the liquid phase, i.e., Eqs. (6)–(8), are solved with the first-order implicit Euler method and the gas properties at the droplet locations (e.g., $\mathbf{u}_{@d}$ and $T_{@d}$) are calculated by linear interpolation. Two-way coupling between the gas and liquid phases about species, mass, momentum, and energy exchanges is performed for each time step.

It should be acknowledged that our understanding of turbulence–detonation interactions is still limited, although turbulence is ubiquitous in real RDE combustors. This is associated with the extreme nature of the detonative flow field, which is characterized by extremely

TABLE I. Chemical reactions for *n*-C₇H₁₆ oxidation (units in cm s mole cal K).

	Reaction	A	n	E_a	a	b	References
I	$2n\text{-C}_7\text{H}_{16} + 15\text{O}_2 \Rightarrow 14\text{CO} + 16\text{H}_2\text{O}$	6.3×10^{11}	0.0	30 000.0	0.25	1.5	34
II	$2n\text{-C}_7\text{H}_{16}(\text{v}) + 15\text{O}_2 \Rightarrow 14\text{CO} + 16\text{H}_2\text{O}$	6.3×10^{11}	0.0	30 000.0	0.25	1.5	34
III	$2\text{CO} + \text{O}_2 \rightleftharpoons 2\text{CO}_2$	4.5×10^{10}	0.0	20 000.0	1.0	0.5	35

high pressure, temperature, and strong isochoric chemical heat release. These make them probably different from the classical Kolmogorov-turbulence.³⁸ Direct numerical simulation of rotating detonation combustion is still not affordable so far. Moreover, it may be questionable to use a classical turbulence model, originally developed for low-Mach-number flows, in RDE modeling. The development of turbulence models for detonations is an important area of detonation studies and still needs considerable future efforts.

III. PHYSICAL MODEL

A. Two-phase rotating detonation model

Figure 1 shows the schematic of rotating detonation in a two-dimensional unrolled model RDE chamber. For simplicity, the upstream plenum is not considered, since only the detonation in the chamber is relevant in this work. The sizes of the domain are 153 mm and 50 mm in x - and y -directions, respectively. This extent ensures that the rotating detonation wave and accompanied flow features (e.g., oblique shock, slip line, and deflagration surface) can be correctly captured. The effects of the model chamber length are analyzed (see the Appendix B) by doubling it to 306 mm (x direction), and it is demonstrated that the two-phase RDC features would not be changed qualitatively with increased combustor length.

The boundary conditions are marked in Fig. 1. Specifically, the outlet is nonreflective, to avoid the backpropagation of the pressure wave or other perturbations from the outlet toward the upstream near the head end, where the RDW and deflagration surface reside. The boundary conditions for the left and right sides are periodic, such that the rotating detonation wave can continuously propagate through the flattened domain.

Partially prevaporized n -heptane sprays are injected into the domain via the continuous inlet at the head end (as shown in Fig. 1), and the fuel is hybrid, composed of n -C₇H₁₆ vapor and liquid n -C₇H₁₆ droplets. The fuel injection condition will be detailed in Sec. III B. Also, the prevaporized n -C₇H₁₆ is assumed to be well mixed with the carrier gas, air, before they are injected into the chamber. Hereafter, the prevaporized n -C₇H₁₆ and air premixture is termed as *prevaporized gas* for brevity. Also, to be readily distinguished, the gaseous n -C₇H₁₆ from prevaporization is termed as “prevaporized n -C₇H₁₆,” whereas that from the *in situ* droplet evaporation in the RDE chamber is “ n -C₆H₁₇ vapor.” Their formulas, respectively, correspond to n -C₇H₁₆ and “ n -C₇H₁₆(v).”

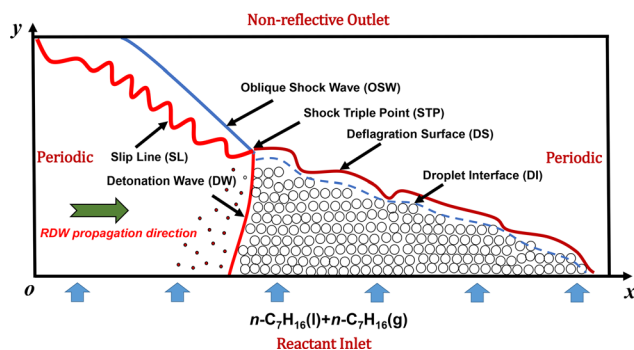


FIG. 1. Schematic of rotating detonation with liquid fuel sprays in a 2D unrolled chamber.

The liquid fuel droplets are monodispersed with an initial diameter being $5\ \mu\text{m}$. Also, different degrees of n -heptane prevaporization are considered, which are parameterized by prevaporized gas equivalence ratio ϕ_g (calculated based on prevaporized n -heptane and air). To examine how the reactant preheating temperature affects the spray RDC, various total temperatures T_g of the injected prevaporized gas are considered. They will be detailed in Sec. III B. Moreover, the total injection pressure of the premixed gas is fixed to be 20 atm in all our simulations. Variations of the total pressure may lead to different rotating detonation behaviors,²⁹ but their effects will not be studied in this work.

The inlet mass flow rates of n -heptane vapor and air are determined by injection total pressure and local pressure near the inlet based on the isentropic expansion relations.^{39–42} For n -heptane droplets, kinematic equilibrium between the gas and liquid phases is assumed, such that the droplets have the same injection velocity as that of the n -heptane vapor. This is practically possible, particularly when the injection plenum connected with the RDE facility is sufficiently long and hence the interphase momentum relaxation can be completed.⁴³ More detailed information about injection conditions can be found in our previous work.²³

Initially (at $t = 0$), the domain in Fig. 1 is filled with standard air (1 atm and 300 K). To initiate the detonation wave, a fresh reactant layer ($153\ \text{mm} \times 12\ \text{mm}$) with stoichiometric gaseous n -heptane/air premixture is patched near the inlet for detonation initiation. One rectangular ignition spot (20 atm and 2000 K, $1\ \text{mm} \times 12\ \text{mm}$) is applied near the left boundary. Within the first cycle, the left and right boundaries are assumed to be solid walls, to avoid two detonation waves propagating oppositely in the combustor. When the right propagating detonation wave is close to the right boundary, both left and right boundaries are changed to periodic condition. Therefore, in the subsequent cycles, the RDW can continuously propagate across the domain.

The computational domain in Fig. 1 is discretized with Cartesian cells. Uniform cells are distributed along x direction and the spacing is $\Delta x = 50\ \mu\text{m}$. Moreover, the cells are stretched along y direction. Specifically, the grid size gradually increases toward the outlet and the ratio of maximum (downstream) to minimum cell sizes (upstream) is 10, which leads to an averaged cell size of $\Delta y = 50\ \mu\text{m}$ near the head end of the model RDE chamber. Since the Lagrangian tracking in our work is based on point-force assumption, the droplet diameter is supposed to be smaller than the cell size, to ensure that the interpolated gas phase quantities at the droplet location (e.g., $\mathbf{u}_{@d}$ and $T_{@d}$) can well approximate those along the droplet surface.²⁴ This essentially leads to the fact that the Lagrangian fuel droplets are not resolved by the Eulerian mesh in our modeling strategy and therefore are at a subgrid scale. With this rationale, the Eulerian mesh resolution Δx and Δy ($50\ \mu\text{m}$) are larger than the Lagrangian droplet diameter (i.e., $5\ \mu\text{m}$ in this work). Mesh sensitivity analysis is performed with three grid sizes, and their total grid numbers are 12×10^6 ($25\ \mu\text{m}$), 3×10^6 ($50\ \mu\text{m}$), and 0.75×10^6 ($100\ \mu\text{m}$). The results (Appendix C) show that the resolution of $50\ \mu\text{m}$ can accurately capture the RDW and droplet dynamics. Further increased mesh resolution does not change the main flow and combustion features of the liquid fuel rotating detonations. Therefore, the mesh with 3×10^6 ($50\ \mu\text{m}$) cells will be selected for our following simulations of two-phase rotating detonations.

TABLE II. Simulated liquid fuel RDC cases.

Case	Gas phase			Liquid phase			
	T_g (K)	ϕ_g	$\dot{m}_{C_7H_{16},g}$ (kg/s)	ϕ_l	$\dot{m}_{C_7H_{16},d}$ (kg/s)	α	d_d^0 (μm)
1	300	0.8	0.263	0.066	0.025	2.5×10^{-4}	5
2	400	0.8	0.246	0.095	0.029		
3		0.7	0.265	0.094	0.033		
4		0.65	0.3	0.09	0.036		
5	500	0.8	0.365	0.128	0.042		

B. Simulation case

Table II shows five cases characterized by different prevaporized gas temperatures (T_g) and equivalence ratios (ϕ_l and ϕ_g). Liquid droplet (ϕ_l) and prevaporized gas (ϕ_g) equivalence ratios are calculated based on the mass of *n*-heptane sprays and gasified *n*-heptane, respectively, as well as the oxidizer from the prevaporized gas. Moreover, the global equivalence ratio (ϕ_l) can be obtained through $\phi_l = \phi_g + \phi_l$.

The liquid phase volume fraction (α) and initial diameter (d_d^0) of the injected fuel droplets are fixed to be 2.5×10^{-4} and $5 \mu\text{m}$ in our simulations, respectively. To account for the influence of propellant preheating and liquid fuel prevaporization, various values of T_g and ϕ_g will be investigated in this work. As shown in Table II, cases 1, 2, and 5 have the same prevaporized gas equivalence ratio ($\phi_g = 0.8$), but the temperature T_g increases from 300 K to 500 K. As for cases 2, 3, and 4, they have the same prevaporized gas temperature ($T_g = 400$ K), but the prevaporized gas equivalence ratio ϕ_g gradually decreases from 0.8 to 0.65.

Moreover, the mass flow rates of prevaporized and liquid *n*-heptane are also detailed in Table II. They are, respectively, estimated based on the mass flow rate $\dot{m}_{total,g}$ of the total injected gas and the liquid phase volume fraction α . Apparently, the prevaporized *n*-heptane mass flow rate $\dot{m}_{C_7H_{16},g}$ is calculated by $\dot{m}_{total,g}$ and the mass fraction of prevaporized *n*-heptane. That for liquid *n*-heptane, $\dot{m}_{C_7H_{16},d}$ is calculated according to the total injected gas volume flow rate $V_{total,g}$ multiplied by the droplet volume fraction α and liquid *n*-heptane material density ρ_d .

IV. RESULTS AND DISCUSSION

A. General characteristics

Figure 2 shows the contours of gas temperature overlaid by *n*-C₇H₁₆ Lagrangian droplets, *n*-C₇H₁₆ vapor mass fraction, pressure, and its gradient magnitude, respectively. The results in this subsection correspond to 1000 μm after the ignition, approximately, and the detonation wave has traveled in the computational domain over 10 cycles. The droplets in Fig. 2(a) are colored by droplet diameter. The results are from case 2 ($T_g = 400$ K and $\phi_g = 0.8$). It is seen from Fig. 2(a) that the droplets are mainly distributed in the triangular fuel refill zone, and their diameters show limited changes due to weak evaporation therein. It should be mentioned that although the reactants are preheated, the static temperatures in the refill zone are still low, ranging from 320 K to 380 K, and the fuel droplets fail to pronouncedly initiate the evaporation process. However, close to the deflagration surface [(DS) in Fig. 2(a)], evaporation of *n*-heptane droplets appreciably increases. This results in a vapor layer [(VL) in Fig. 2(a)] between

the DS and droplet-laden area in the refill zone. Additionally, a portion of the fuel droplets survive in the postdetonation region (indicated by the white arrow) and the droplet diameters are quickly reduced after they travel through the detonation front due to the strong evaporation rate caused by the high local gas temperature (over 3000 K), as shown in Fig. 2(a).

It can be seen in Fig. 2(b) that a high concentration of *n*-C₇H₁₆ vapor due to the droplet *in situ* evaporation in the RDE chamber can be observed in the vapor layer. This is because the injected droplets move dominantly along the *y*-direction in the refill zone, as unveiled by our recent work based on the droplet trajectory analysis.²³ Hence, those at the top of the droplet-laden area generally have a relatively longer residence time in the RDE chamber, and they interact with the hot DS immediately after they are injected. Ahead of the RDW, the thickness of the vapor layer is increased to about 25% of the local height of the fuel refill zone. Also, the morphology and stability of the DS are strongly affected by the blast waves [(BW) in Fig. 2(d)].²⁹ Note that these blast waves are emanated from the shock triple point, caused by the local acoustic impedance of the fresh and burned gas demarcated by the DS to the RDW.⁴⁴ One can see from Fig. 2(d) that some

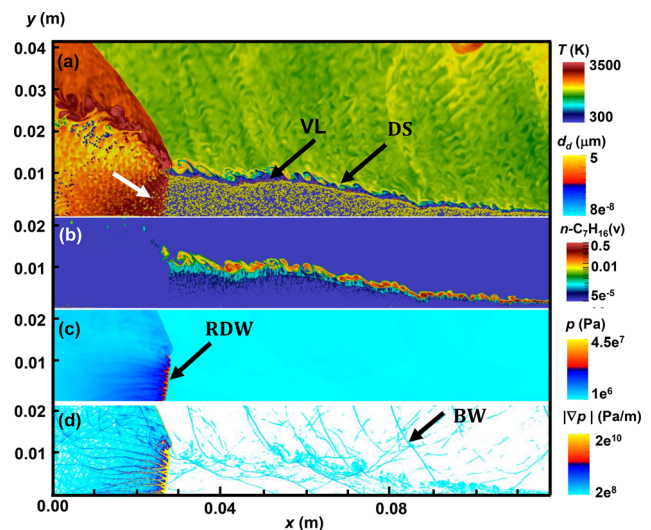


FIG. 2. Contours of (a) gas temperature with *n*-C₇H₁₆ droplets, (b) *n*-C₇H₁₆ vapor mass fraction, (c) pressure, and (d) magnitude of pressure gradient. Results from case 2: $T_g = 400$ K and $\phi_g = 0.8$. VL: vapor layer, DS: deflagration surface, BW: blast wave.

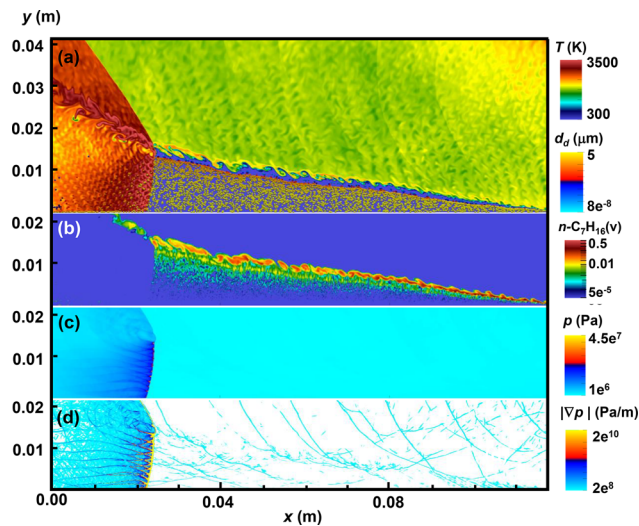


FIG. 3. Contours of (a) gas temperature with n -C₇H₁₆ droplets, (b) n -C₇H₁₆ vapor mass fraction, (c) pressure, and (d) magnitude of the pressure gradient. Results from case 5: $T_g = 500$ K and $\phi_g = 0.8$.

of the blast waves are transmitted through the DS and continuously propagating in the refill zone, inclined with respect to the RDW. These blast waves may further influence the evaporating droplets inside the fuel refill zone and this will be further discussed in Figs. 5–7.

Likewise, the counterpart results from case 5 are shown in Fig. 3, with $\phi_g = 0.8$ and increased prevaporized gas temperature $T_g = 500$ K. Stronger evaporation occurs in the refill zone, which leads to more distributed gaseous n -C₇H₁₆ therein compared to that in Fig. 2(b). For droplets from the same injection location, when they cross the refill zone, their evaporation starts spatially earlier than in Fig. 2(b), corresponding to half height of the refill zone. Also, more leakage of unburned n -C₇H₁₆ vapor from the shock triple point can be found. For higher reactant temperature (500 K) in Fig. 3, the peak pressures at the RDW are lower than those in Fig. 2(c) with $T_g = 400$ K, because of the reduced volumetric energy density of the detonable gas when the gas temperature is elevated.⁴⁵

Figure 4 shows the results from case 3 ($T_g = 400$ K and $\phi_g = 0.7$), which is introduced to be compared with Fig. 2 ($\phi_g = 0.8$) about the influence of prevaporized gas equivalence ratio on rotating detonation combustion. The flow structure, detonation wave, droplet, and vapor distributions are qualitatively similar to those in Fig. 2. This indicates that further reduction of prevaporized gas equivalence ratio from 0.8 to 0.7 does not show remarkable effects on the foregoing features. Nevertheless, compared to Fig. 2(a), there are more escaping fuel droplets in the postdetonation region when ϕ_g is reduced, as shown in Fig. 4(a). This implies that low prevaporization (lower ϕ_g) would lead to less *in situ* evaporation within the refill zone and hence insufficient utilization of the liquid fuel. This is because that lower prevaporization degree generally results in a relatively weaker detonation wave, and therefore the droplets are heated more slowly near the detonation wave and are more difficult to be fully vaporized.²³

When the prevaporized gas equivalence ratio is further reduced to $\phi_g = 0.65$ (case 4), the main detonation features have limited differences from those in case 3 (hence not presented here). However, more

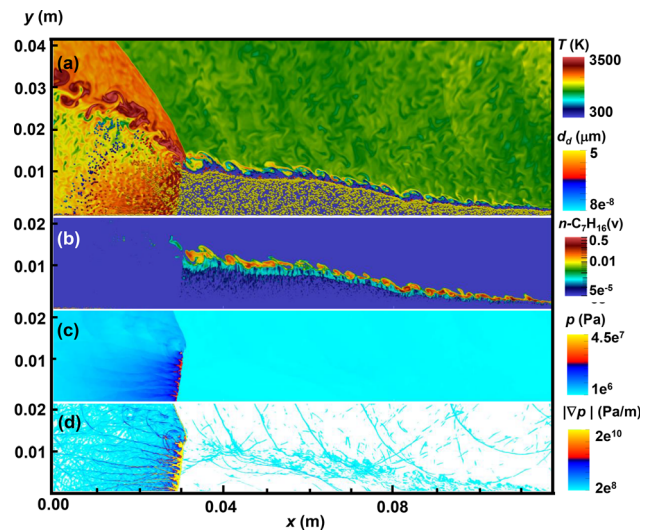


FIG. 4. Contours of (a) gas temperature with n -C₇H₁₆ droplets, (b) n -C₇H₁₆ vapor mass fraction, (c) pressure, and (d) magnitude of pressure gradient. Results from case 3: $T_g = 400$ K and $\phi_g = 0.7$.

residual fuel droplets exist in the postdetonation region. In our simulations, stable RDW cannot be achieved if the prevaporized gas equivalence ratio is reduced to less than 0.65. Therefore, this indicates that without sufficient prevaporization of the liquid fuel, it is difficult to maintain the RDW with liquid n -heptane sprays. For liquid fuel RDEs, how much liquid fuels should be gasified before being injected into the combustor and whether an optimal percentage envelope exists are still open questions and should be further studied.

In Figs. 2(b), 3(b), and 4(b), one can see the mass fractions of n -C₇H₁₆ vapor are high along the convoluted deflagration surface, and the peak values range from 0.4 to 0.5 in these cases. The reader should be reminded that these fuel vapors are visualized fully based on the *in situ* droplet evaporation [i.e., n -C₇H₁₆(v)] in the RDE chamber, excluding the prevaporized ones. This phenomenon is also observed by Hayashi *et al.* in their Eulerian–Eulerian modeling of JP-10/air RDE,²² but they did not explain the underlying mechanisms and the individual droplet distributions cannot be captured due to the Eulerian–Eulerian approach. Based on our studies, the accumulation of the n -heptane vapor is mainly from two possible sources. First, at the right end of the fuel refill zone where the reactant injection is just recovered after the RDW passes, the droplets are injected into the RDE chamber where the denoted products from the last RDW cycle are still close to the inlet. Such intimate interactions with the hot environment lead to fast evaporation of these newly injected droplets. These fuel vapors cannot be deflagrated due to the locally rich composition and instead are transported along the sheared contact surface toward the triple point and oncoming detonation wave. Second, as shown in Figs. 2(b), 3(b), and 4(b), the droplets at the top of the droplet-laden area in the refill zone strongly vaporize, which also contributes toward the vapor accumulation along the deflagration surface. As such, essentially, formation of the high concentration of n -C₇H₁₆ along the contact surface is associated with the early batch of fuel droplets when the fuel inlets are activated. This would affect the

combustion characteristics along the contact surface and therefore may modulate the fraction of the detonated fuels.^{23,32} Ultimately, the RDW consumes part of the vapor near the triple point, while the rest escapes from the refill zone [see Fig. 3(b)]. In implementations of practical liquid fuel RDE's, high concentration of *n*-heptane from droplet evaporation along the DS is supposed to be avoided, since this may deteriorate the overall detonation combustion efficiency and local fuel-rich burning may also lead to generation of the pollutants (e.g., soot, carbon monoxide, or oxides of nitrogen).⁴⁶ A possible solution, but needed to be deliberately designed, is to adjust the timing of liquid fuel injection, to ensure the early batch of the liquid fuel sprays is directly injected into the refill zone, instead of the hot detonated gas.

B. Detailed structure in refill zone

Detailed structure of the flow field and droplet properties in the fuel refill zone will be further discussed in this section. Plotted in Fig. 5(a) is the gas temperature, and the upper limit of the temperature range is clipped to 400 K for a clear demonstration of the refill zone temperature. The black solid line in Fig. 5(a) is the two-phase contact surface (TCS), which is the top layer of the droplet-laden area. The upper boundary of gas temperature contours loosely corresponds to the deflagration surface [i.e., DS in Fig. 5(b)]. Furthermore, we can obviously see the wavy temperature distributions caused by the compression of the blast waves and this can be further confirmed by visualizing the instantaneous blast wave locations with pressure gradient magnitude in Figs. 5(b)–5(f). The low temperature rise behind the blast waves indicates that their intensities are generally weak.

Figures 5(b)–5(f) show the contours of the pressure gradient magnitude overlaid by the Lagrangian droplets with various parameters, including droplet temperature T_d , evaporation rate \dot{m}_d , diameter d_d , Sherwood number Sh , and slip velocity $|\mathbf{u}_{\text{gas}} - \mathbf{u}_d|$. The blast waves have no apparent effects on droplet temperature variations, even if the gas temperature has already increased because of the blast wave as shown in Fig. 5(a). This is reasonable, because there exists a finitely long thermal relaxation time for the droplets to be heated caused by heat exchange with the gas phase. Similar droplet momentum relaxation duration is also observed, which can be confirmed by

the finite slip velocity behind the blast waves in Fig. 5(f). This leads to increased droplet Reynolds number Re_d (results not shown here) and Sherwood number Sh [Fig. 5(e)] of the corresponding droplets. As shown in Fig. 5(c), droplet evaporation rate \dot{m}_d increases behind the blast waves. Based on the results in Figs. 2(a) and 2(e), one can see that this enhancement from the blast waves is associated with the kinematic, instead of thermal, effects. This is also observed by Zhuang *et al.*⁴⁷ in their simulations of detonations in water mists and termed as the Sherwood number effect. Meanwhile, this enhancement only occurs at the upper part of the droplet-laden area, where the fuel droplets have already been heated. Near the fuel injector, limited variations of \dot{m}_d can be seen from Fig. 5(c) due to low droplet temperatures (around 300 K). Although we can observe that the evaporation rate is affected by propagating blast waves, however, the limited fuel sprays are fully vaporized within the droplet-laden area, with less pronounced diameter reduction, as indicated in Fig. 5(b).

Figure 6 shows the close-up view on the vapor layer, deflagration surface, and *n*-C₇H₁₆ droplets (colored by the evaporation rate \dot{m}_d). Figure 6(a) shows the contour of *n*-heptane vapor, *n*-C₇H₁₆(v), near the deflagration surface. When the droplets are closer to the DS, droplet evaporation starts, which leads to isolated or connected high concentration of *n*-heptane vapor around the droplets. Therefore, the concentration of *n*-heptane vapor near the two-phase contact surface is high, and the vapor layer is filled with the nonuniform *n*-heptane. This is also demonstrated in Fig. 2(b). All these vapors contribute toward the high concentration of *n*-heptane along the DS, as discussed in Sec. IV A. One can see from Fig. 6(b) that some residual evaporating droplets are engulfed by the eddies along the DS, visualized by the isolines of λ_2 [the second largest eigenvalue of $\mathbf{S}^2 + \mathbf{W}^2$, $\mathbf{S} = 0.5(\nabla \mathbf{u} + \nabla \mathbf{u}^T)$ and $\mathbf{W} = 0.5(\nabla \mathbf{u} - \nabla \mathbf{u}^T)$] in Fig. 6(b).⁴⁸

The interactions between the blast waves, compressed gas phase, and liquid droplets are also further demonstrated in Figs. 6(c) and 6(d). Although the traveling blast wave encroaches the fuel refill zone, however, the fuel spray droplets do not appreciably move with and therefore follow the blast waves, thereby not resulting in droplet preferential accumulation immediately behind the shock front and shock-driven multiphase instability.^{49–51} This may be because the blast waves

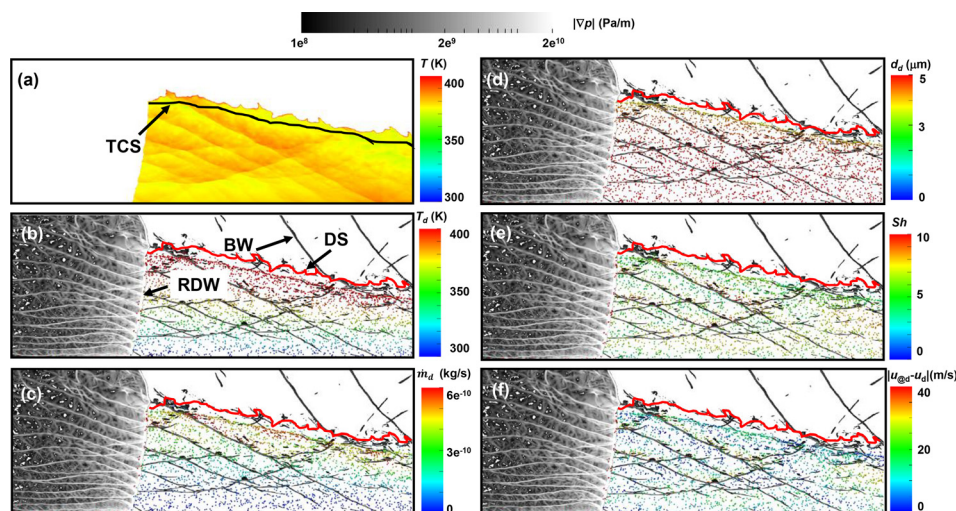


FIG. 5. Interactions between blast waves and fuel droplets in the refill zone: (a) gas temperature, (b) droplet temperature, (c) droplet evaporation rate, (d) droplet diameter, (e) Sherwood number, and (f) velocity difference between droplet and gas phases. Results from case 2. Background contours in Figs. 5(b)–5(f) is pressure gradient magnitude. The black line in Fig. 5(a) is the two-phase contact surface, while the red lines in Figs. 5(b)–5(f) denote the deflagration surface.

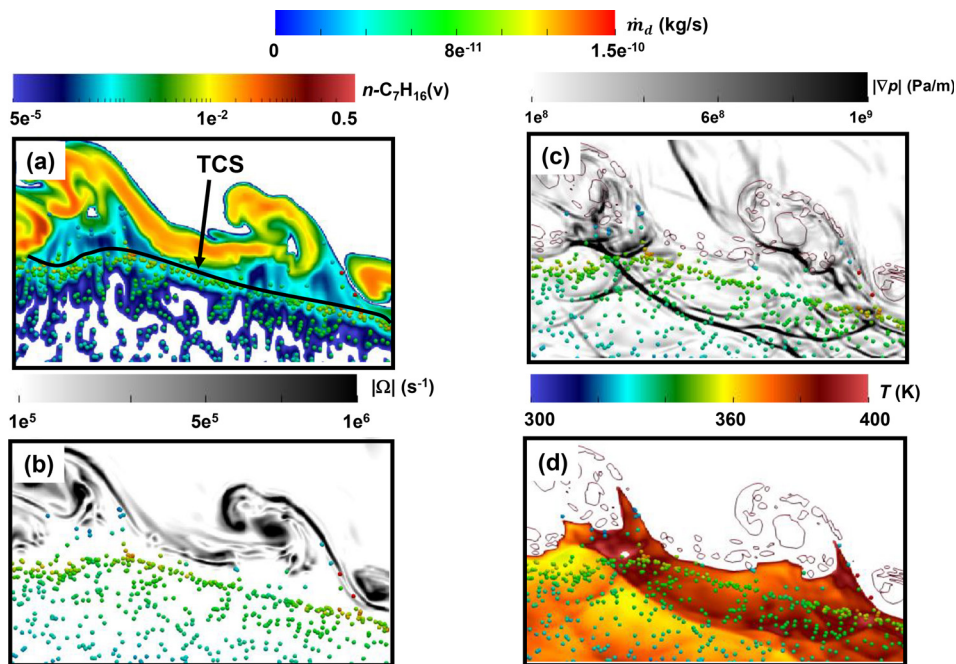


FIG. 6. Close-up view of the vapor layer and deflagration surface: (a) *n*-heptane vapor mass fraction, (b) vorticity magnitude, (c) pressure gradient magnitude, and (d) gas temperature. The Lagrangian droplets are colored by the evaporation rate. Results from case 2. Red isolines in (c) and (d): $\lambda_2 = 1 \times 10^{10} \text{ s}^{-2}$.

are relatively weak and/or the droplet inertial is large. This feature is practically important to attain organized, continuous, and self-sustained rotating detonation combustion with liquid fuel sprays. Any aerodynamic perturbation on the liquid fuel droplets inside the refill zone would affect the nonuniform and/or nonsteady fuel supply for the rotating detonation waves. This may induce adverse outcomes, such as RDW destabilization and even failure, and therefore deteriorate the overall performance of an RDE.

Likewise, Fig. 7 shows the close-up view on the shock triple point of the same case in Fig. 6. Obviously, the droplet evaporation rate considerably increases when they cross the detonation front. No accumulated *n*-heptane vapor around these escaping droplets is observed, due to the local chemical reactions in the denoted gas environment. One can find that part of *n*-heptane vapor near the deflagration surface is consumed near the shock triple point. Nonetheless, some of them leak and are transported downstream along the slip line. The transverse

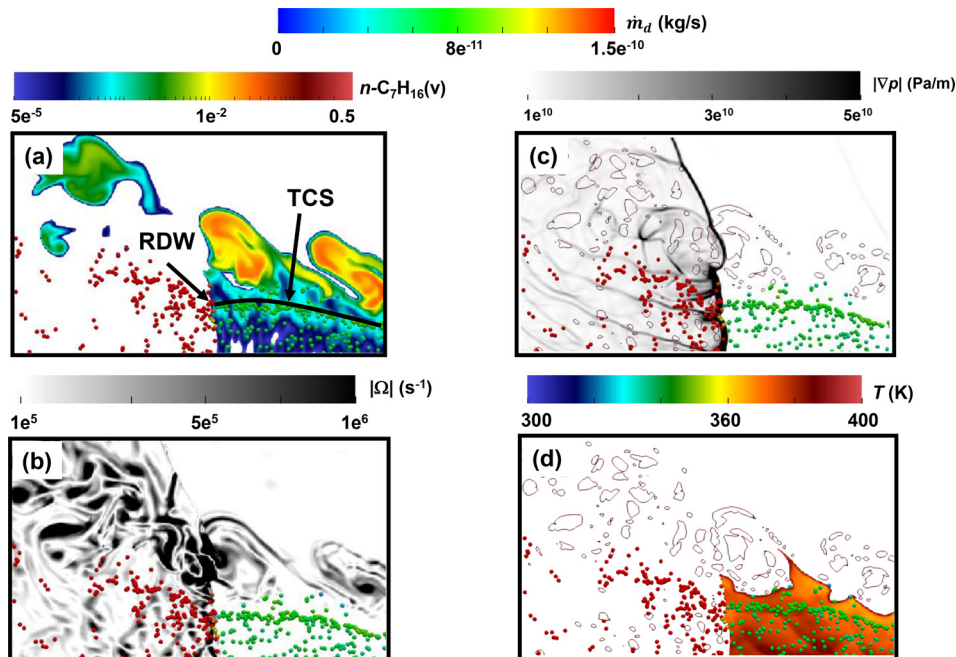


FIG. 7. Close-up view of the shock triple point: (a) *n*-heptane vapor mass fraction, (b) vorticity magnitude, (c) pressure gradient magnitude, and (d) gas temperature. The Lagrangian droplets are colored by the evaporation rate. Results from case 2. Isolines in (c) and (d) are $\lambda_2 = 1 \times 10^{10} \text{ s}^{-2}$.

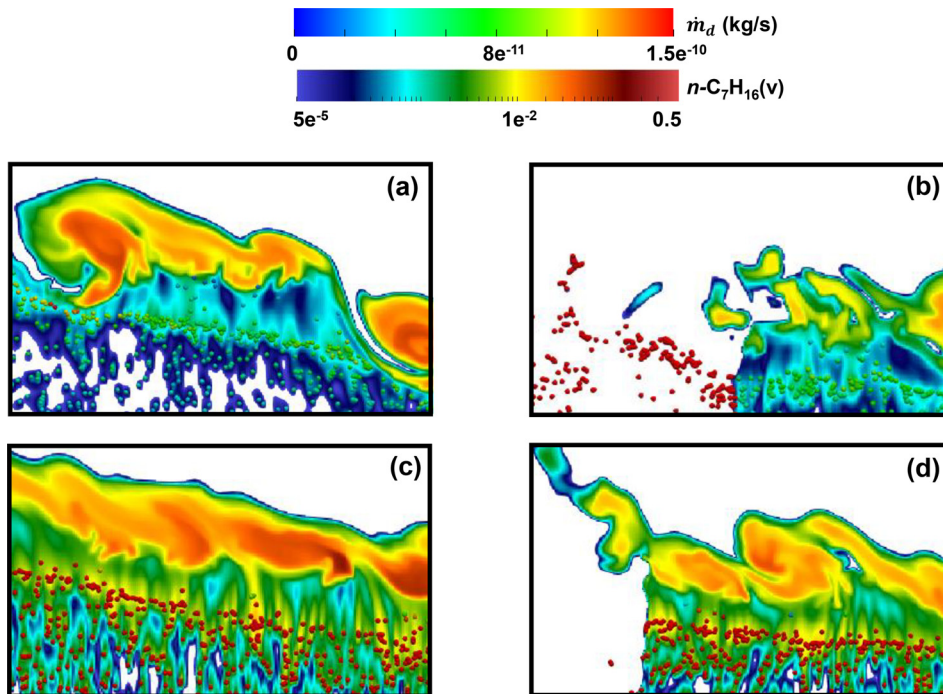


FIG. 8. Close-up view of $n\text{-C}_7\text{H}_{16}$ vapor mass fraction and fuel droplets along (a) and (c) deflagration surface and (b) and (d) shock triple point in case 3 (a) and (b) and case 5 (c) and (d).

and detonation waves are obviously observed, and the transverse wave has limited effects on the droplets in postshock region.

In Figs. 5–7, only case 2 is discussed, and Fig. 8 shows the counterpart structures near the deflagration surface and shock triple point in case 3 ($\phi_g = 0.7$, $T_g = 400$ K) and case 5 ($\phi_g = 0.8$, $T_g = 500$ K). Comparing Figs. 6(a) and 8(a), as well as Figs. 7(a) and 8(b), one can find that the distributions of n -heptane vapor and droplet distributions are generally similar. This indicates that the variations of the prevaporized gas equivalence ratio from 0.8 to 0.7 do not significantly affect the above aspects. However, the changes of gas temperature, from 400 K to 500 K, considerably influence the droplet evaporation in the refill zone, as shown in Figs. 8(c) and 8(d). These observations are consistent with those in Sec. IV A, based on Figs. 2–4.

C. Further interpretations of layered characteristics of fuel sprays

Based on the results in Secs. IV A and IV B, in Fig. 9, we further sketch the conceptual model of layered distributions of liquid droplets and gaseous vapor in the fuel refill zone of rotating detonation. Specifically, they include cold sprays from the liquid fuel injectors (marked with I in Fig. 9), heated and evaporating sprays (II), and vapor layer (III). Above the vapor layer, there is the deflagration surface (or contact surface) where considerable vapor accumulation can be found. The properties of the carrier gas and liquid fuel droplets would affect the distributions of the above zones I, II, and III. For cold sprays, it takes finitely long time (corresponding to zones I and II) for them to be heated and then vaporize. Ideally, zone III is supposed to be maximized in the refill zone, which means the high fuel vapor concentration therein. These vapors can be consumed by the RDW and therefore is beneficial for the detonative combustion.

One can see from Secs. IV A and IV B that the kinetic contributions of liquid fuels toward the rotating detonations can be categorized as (1) evaporation in the refill zone before the RDW arrives and (2) evaporation around the RDW front. For the former, finitely long time is required for the liquid fuels to be converted into detonable gas, while for the latter, it is more instant and only occurs when the propagating RDW sweeps the droplets, through direct two-phase interactions (e.g., drag, pressure gradient, and strong convective heat transfer). Based on the droplet size in this study, when the droplets cross the RDW, strong droplet evaporation proceeds. However, whether there is a critical droplet diameter with which they can be effectively consumed by the RDW and how the vapor inhomogeneity (imperfectly reactant mixing around the detonation wave) affects the instantaneous detonation dynamics need future investigations.

Moreover, in the first category, if the distance between the individual droplets and the RDW is L_d , then the duration for the latter to approach the droplets is about $\tau_{det} = L_d/D_{det}$ (D_{det} is the averaged

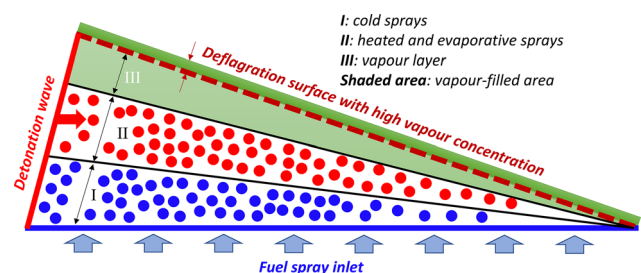


FIG. 9. Conceptual model of distributions of liquid fuel sprays and vapor in the refill zone of rotating detonation.

RDW propagation speed).²³ To have sufficiently detonable gas in the refill zone, within this period, there is a sequence of processes to be completed, including droplet heating, evaporation, and reactant mixing. The droplet heating and evaporation in the refill zone will be

further discussed in Sec. IV D. Unfortunately, for the droplets injected close to the RDW, limited time is available for them to be fully heated, let alone evaporation. Their kinetic contributions toward the detonation wave depend on whether they can be quickly consumed by the RDW; otherwise, deflagrative combustion can proceed in the detonated gas or the residue droplets exit from the RDE chamber.

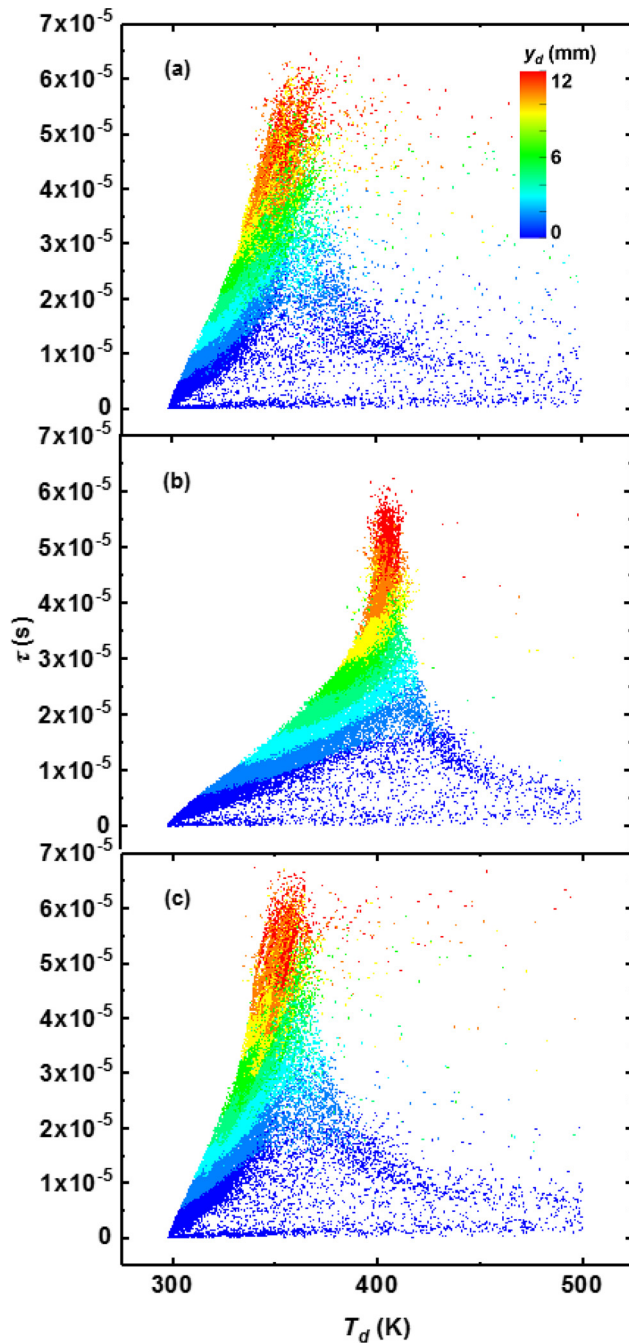


FIG. 10. Scatters of droplet temperature vs droplet residence time in the refill zone: (a) $T_d = 400$ K and $\phi_g = 0.8$ (case 2); (b) $T_d = 500$ K and $\phi_g = 0.8$ (case 5); (c) $T_d = 400$ K and $\phi_g = 0.7$ (case 3).

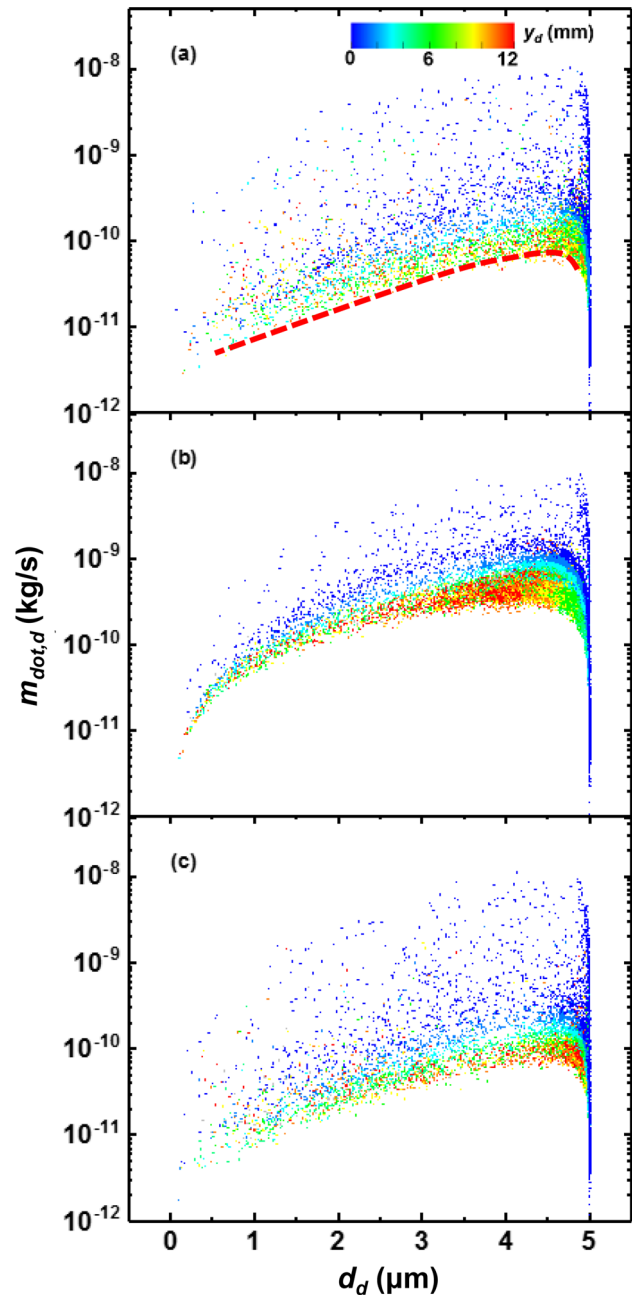


FIG. 11. Scatters of droplet evaporation rate vs droplet diameter in the refill zone: (a) $T_d = 400$ K and $\phi_g = 0.8$ (case 2); (b) $T_d = 500$ K and $\phi_g = 0.8$ (case 5); (c) $T_d = 400$ K and $\phi_g = 0.7$ (case 3).

Although more complicated factors exist in practical liquid fuel RDEs, such as turbulence, three-dimensionality, and liquid fuel atomization/breakup, however, the conceptual model in Fig. 9 provides a physical guidance and insight into implement rotating detonations with liquid fuels.

D. Droplet heating and evaporation in the refill zone

Figure 10 shows the scatters of droplet temperature (T_d) vs droplet residence time (τ) in the refill zone. The results in Figs. 10(a)–10(c) are, respectively, from cases 2, 5, and 3. The scatters are colored by their y -direction coordinates y_d . The droplet temperature increases when the droplet residence time increases. This indicates that the droplets are continuously heated by the preheating gas when they move downstream from the inlet. The scatters near the top (red color) have the longest residence time in the refill zone and the largest height (around 12 mm). This approximately corresponds to the detonation wave height and those droplets are close to the shock triple point connecting the RDW, DS, and the oblique shock (see Fig. 1). However, the temperatures of the droplets with the longest residence time are different. Specifically, when the prevaporized gas temperature is 400 K in Figs. 10(a) and 10(c), the droplet temperature can be up to 350 K, while for the gas temperature is 500 K, it is around 400 K [see Fig. 10(b)]. Note that the averaged gas temperature in the refill zone is about 380 K (in cases 2 and 3) and 470 K (in case 5) in the refill zone, which means that the droplets near the shock triple point have been close to the gas

temperature and hence reached interphase thermal equilibrium. However, their temperatures are still lower than the boiling point (about 540 K) under the local conditions.

Furthermore, in Figs. 10(a) and 10(c), we can find that the temperatures of some droplets are higher than the prevaporized gas temperature, i.e., 400 K, and can be up to $T_d = 500$ K. Their temperatures are close to the boiling point and therefore strong evaporation proceeds. These droplets generally have shorter residence times ($\tau \leq 20 \mu\text{s}$). This indicates that they are freshly injected from the inlet and have been quickly heated by the detonated gas. They correspond to the first batch of the fuel spray injection and lie near the two-phase contact surface (denoted with TCS in Figs. 5–7). They make significant contributions toward the formation of high vapor concentration along the deflagration surface, as discussed in Sec. IV B. For those droplets with the intermediate location y_d , the droplet temperature increases with y_d , because of the heating by the hot gas. It should be clarified that the same scatter color generally represents the droplets in a range of y location (3 mm for each color), so the scatters with the same color are distributed when they are plotted vs the droplet temperature. The droplet temperature increases with droplet residence time and hence the scatters in the same color are strip-shaped in Fig. 10.

Figures 11(a)–11(c) show the scatters of the droplet evaporation rate (\dot{m}_d) vs the droplet diameter (d_d) in the refill zone in cases 2, 5, and 3. They are also colored by the y -direction location y_d . We can

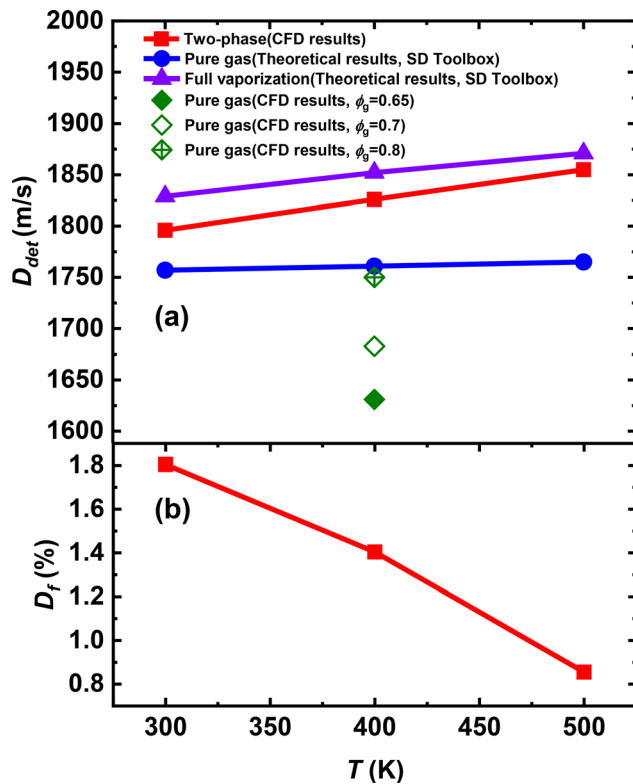


FIG. 12. (a) Detonation propagation speed and (b) deficit as functions of prevaporized gas temperature.

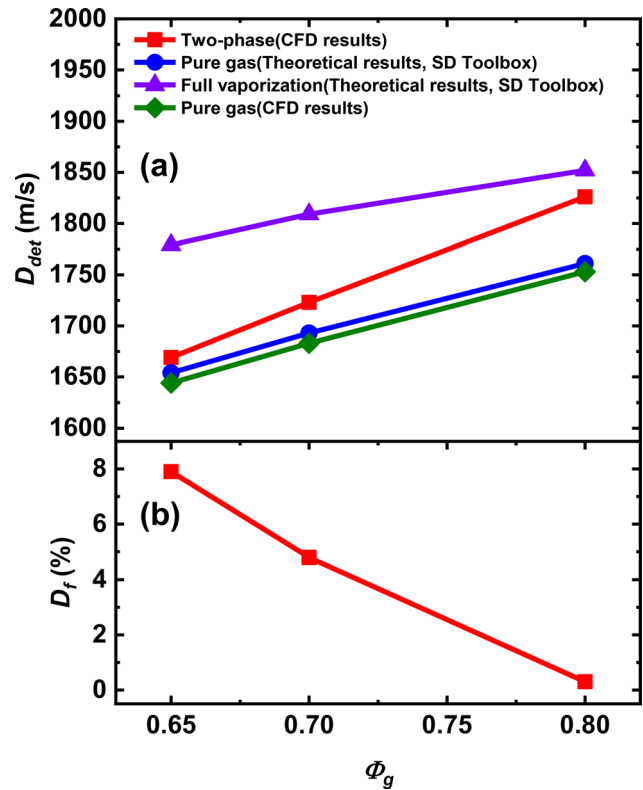


FIG. 13. (a) Detonation propagation speed and (b) deficit as functions of prevaporized gas equivalence ratio.

observe that the droplets with a high evaporation rate \dot{m}_d have relatively low y_d and meanwhile their corresponding diameters d_d are more distributed, from the initial droplet diameters to very small ones. Those droplets with an initial diameter (about $5\ \mu\text{m}$) correspond to those initially injected from the inlet and interact closely with the hot product gas. In general, for high prevaporized gas temperature [e.g., 500 K in Fig. 11(b)], the whole scatters lie at higher locations than those with low reactant temperature [e.g., 300 K in Fig. 11(a)], which means that the droplet evaporation rates are generally higher. The upper, but sparser, scatters in Figs. 11(a)–11(c) correspond to those near the deflagration surface. The lower scatters show obvious differences and \dot{m}_d is the highest for these scatters in Fig. 11(b), because of the high preheating temperature, which means that the concentration of scatters near the dashed line is high than that in Figs. 11(a) and 11(b) when the total scatters are close. Moreover, there are limited differences between Figs. 11(a) and 11(c) because their prevaporized gas temperatures are the same.

E. Detonation speed

The effects of the prevaporized gas temperature and equivalence ratio on rotating detonations will be discussed in this section. Figure 12 shows the average detonation speed and deficit as functions of different prevaporized gas temperatures. The two-phase cases correspond to the numerical simulations in the current study. Pure gas cases (theoretical results) are the calculations based on the SD Toolbox³⁷ and only prevaporized gaseous $n\text{-C}_7\text{H}_{16}$ (no liquid droplets) are considered. Pure gas cases (CFD results) are from numerical simulations with only prevaporized gaseous $n\text{-C}_7\text{H}_{16}$ (no liquid droplets). The full vaporization cases are also calculated with the SD toolbox, but the gas compositions

are estimated by assuming that all the $n\text{-C}_7\text{H}_{16}$ sprays are vaporized in the mixture.

As shown in Fig. 12, detonation propagation speed D_{det} in two-phase RDC lies between the theoretical results (with SD Toolbox) from pure gas and full vaporization cases. This is because all the current cases are under fuel-lean conditions (see Table II) and evaporation of liquid $n\text{-C}_7\text{H}_{16}$ sprays makes the total equivalence ratio of the detonable mixture closer to stoichiometric condition. Therefore, the theoretical cases with fully vaporized $n\text{-heptane}$ have the highest detonation speed. Due to the existence of the $n\text{-C}_7\text{H}_{16}$ droplets, the computed detonation propagation speeds from two-phase RDC are slightly lower than the results in the full vaporization cases but higher than those in pure gas cases from SD Toolbox. Also, due to increased reactant temperatures from 300 K to 500 K, the two-phase detonation speed increases. The greater sensitivity of the detonation wave propagation in two-phase RDC to the reactant temperature can be found in Fig. 12(a), characterized by the larger slope in the $D_{det} - T$ diagram. The rotating detonations with only prevaporized $n\text{-heptane}$ are also simulated with the same configuration in Fig. 1. With increased ϕ_g , the detonation propagation speed increases. Also, the detonation speed in pure gas (CFD results, $\phi_g = 0.8$) case is very close to the corresponding theoretical results because of the homogeneous (purely gas) reactants ahead of the RDW. Moreover, velocity deficit D_f of the two-phase RDW propagation speed D_{det} in Fig. 12(b) is estimated based on the full vaporization cases in Fig. 12(a). Apparently, D_f decreases as the reactant temperature increases from 300 K to 500 K. This is reasonable since higher reactant temperature generally results in more droplet evaporation inside the refill zone, as shown in the results of Secs. IV A and IV B.

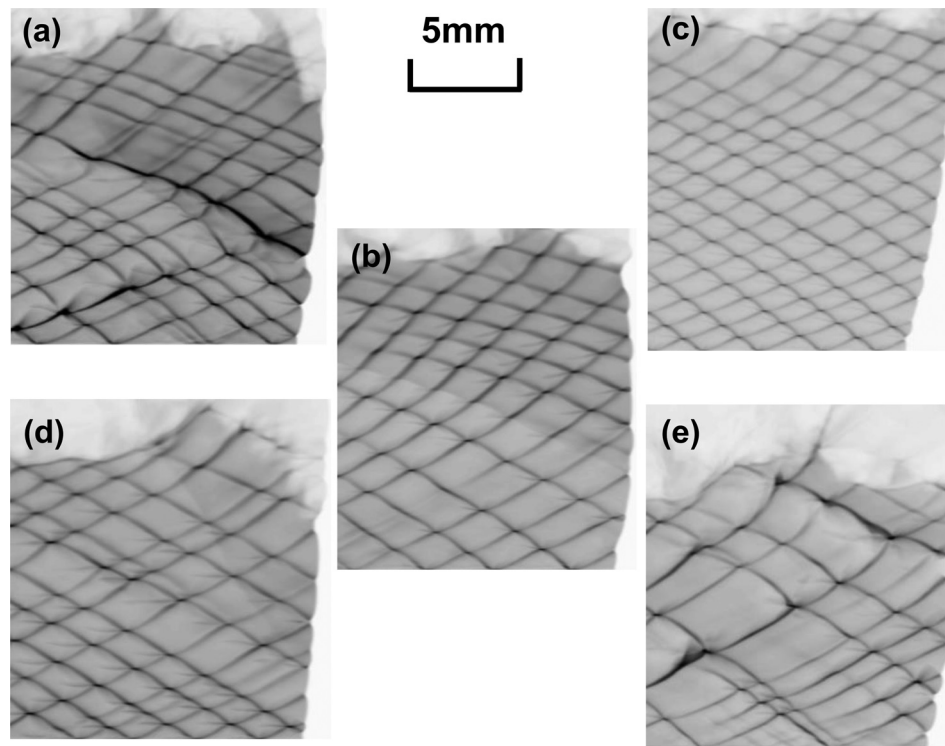


FIG. 14. Trajectories of peak pressure: (a) $T=300\text{ K}$ and $\phi_g=0.8$; (b) $T=400\text{ K}$ and $\phi_g=0.8$; (c) $T=500\text{ K}$ and $\phi_g=0.8$; (d) $T=400\text{ K}$ and $\phi_g=0.7$; (e) $T=400\text{ K}$ and $\phi_g=0.65$. Image size is $0.0132\text{ m} \times 0.0136\text{ m}$.

Figure 13 shows the variations of the detonation propagation speed with different prevaporized gas equivalence ratios (ϕ_g). The computed speeds in the two-phase RDC are between the full vaporization and pure gas results. Moreover, they have the largest slope, indicating the favorable effects of higher ϕ_g on two-phase RDW propagation. Higher prevaporized gas equivalence ratio ϕ_g can support stronger RDW, and when the n -C₇H₁₆ droplets cross the detonation fronts more droplets can be gasified and consumed by the detonation wave.²³ Therefore, the detonation speed deficit decreases with the prevaporized gas equivalence ratio. The detonation speeds from the pure gas cases from SD Toolbox and CFD results have a similar trend and they are close because of the homogeneous gaseous reactant ahead of RDW in the CFD calculations.

F. Detonation cell size

Figure 14 shows the numerical soot foils of rotating detonations with different prevaporized gas temperatures and equivalence ratios. The cells in Fig. 14 are recorded from the trajectories of peak pressure, corresponding to the triple points connecting the Mach stem, incident wave, and transverse shock wave along the detonation front. Note that the lower boundary of each figure corresponds to the reactant inlet. It is suppressed immediately behind the detonation waves (since the local pressure near the inlet is lower than the total pressure) and assumed to be nonpenetrating walls in our simulations.²³ Therefore, the transverse waves (hence triple points) are reflected when they reach the inlet. Nevertheless, when the moving transverse waves arrive at the shock triple point (connection of detonation, oblique shock, and deflagration surface, see the notation in Fig. 1), the transmission of the transverse waves occurs, which can be shown by the light gray trajectories near the upper boundaries of the numerical soot foils. They, therefore, escape from the detonation front and imping the oblique shock wave. Nevertheless, part of the transverse wave is reflected from the deflagration surface, which can be observed by the downward movement of the triple points along the detonation wave. It has been shown that the continuous reflection of the transverse wave from the triple point at the top of the RDW front is critical for sustaining stable detonation propagation.²²

We first focus on Figs. 14(a)–14(c), which have the same prevaporized gas equivalence ratio (0.8) but different reactant temperatures (300, 400, and 500 K, respectively). It is seen that generally the detonation cell size decreases and becomes more uniform as reactant temperature increases from 300 K to 500 K. This means that the detonable gaseous mixture is more reactive due to higher temperature and also n -C₇H₁₆ vapor addition, and hence there are more triple points along the detonation front. For Figs. 14(b), 14(d), and 14(e), they have the same gas temperature (400 K) but different prevaporized gas equivalence ratios (0.8, 0.7, and 0.65, respectively). Obviously, the cell size and irregularity increase when ϕ_g decreases, which implies that the rotating detonations are more unstable when the prevaporization degree is lowered. This may be also affected by the *in situ* droplet evaporation, since the lower ϕ_g also reduces the droplet evaporation near the detonation wave.²³ The influences of the droplet addition on detonation cell sizes are also shown through the comparisons with the cell sizes of the droplet-free mixtures (see the Appendix D).

V. CONCLUSIONS

Two-dimensional rotating detonations fueled by partially prevaporized n -heptane sprays are simulated with the hybrid Eulerian–Lagrangian method. A flattened domain with periodic

boundaries is considered to mimic the annular rotating detonation combustor. Emphasis is laid on the effects of prevaporized gas temperature and equivalence ratio on fuel droplets and vapor distributions in the fuel refill zone. Also, their effects on detonation propagation speed and cell sizes are also discussed. The main conclusions are summarized as below.

Increasing the prevaporized gas temperature significantly promotes the droplets vaporization in the refill zone and their evaporation

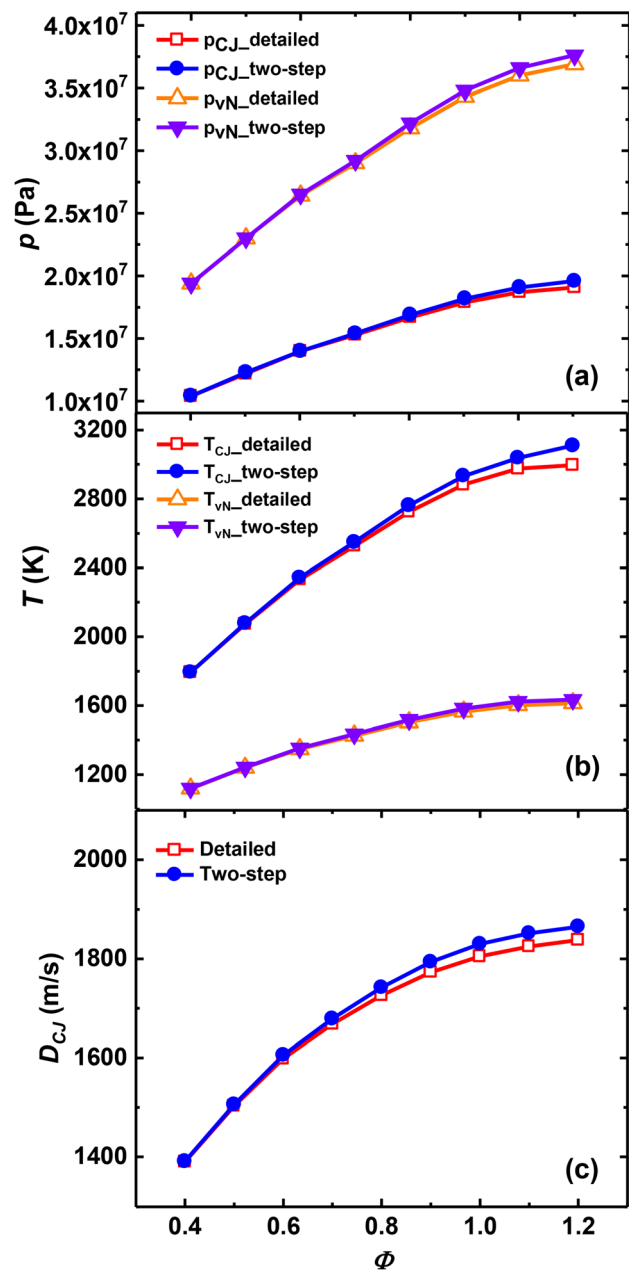


FIG. 15. Comparisons of the two-step^{34,35} and detailed³⁶ chemical mechanisms: (a) pressure, (b) temperature, and (c) propagation speed.

rates are high near the deflagration surface, because they are heated by the local high temperature. Freshly injected droplets at the right end of the refill zone have strong evaporation since they directly interact with the hot product. A vapor layer is formed between the deflagration surface and the two-phase contact surface. High mass fraction of *n*-heptane vapor can be found along the deflagration surface. These *n*-heptane vapors cannot be fully consumed by the detonation wave and triple point because of high fuel concentration. A conceptual model is proposed for the layered distributions of the liquid fuel sprays with spatially evolving properties in the refill zone. Also, the blast waves can penetrate through the deflagration surface into the refill zone and further influence the local droplet thermodynamic properties. The droplet evaporation rate increases behind the blast waves due to the kinematic effects, but it has limited effects on the variations of local droplet temperature and diameter.

Also, the detonation propagation speed increases as the prevaporized gas temperature and/or *n*-heptane prevaporized equivalence ratio increase. The detonation cell size decreases and becomes more uniform as the reactant temperature increases because more *n*-heptane droplets have already vaporized and the perturbation from the droplet vaporization is also reduced. It is also observed that the cell size and irregularity increase when the prevaporized equivalence ratio decreases.

ACKNOWLEDGMENTS

This work used the computational resources of the National Supercomputing Centre, Singapore (<https://www.nsc.sg>). Q.M. is supported by the China Scholarship Council (No. 201906680008) and the Open Research Grant (No. KFJJ20-09M) from State Key Laboratory of Explosion Science and Technology, Beijing Institute of Technology. N.Z. is supported by National Nature Science Foundation of China (Grant No. 52071103).

APPENDIX A: VALIDATION OF TWO-STEP CHEMISTRY

Validations are made for the two-step chemical mechanism^{34,35} listed in Table I and Fig. 15 compares the Chapman–Jouguet and von Neumann parameters as well as detonation propagation speed predicted with two-step and detailed mechanisms.³⁶ In general, the parameters from both mechanisms are close over the shown equivalence

ratios, i.e., 0.4–1.2. Therefore, the two-step mechanism is accurate to predict the key detonation relevant properties.

APPENDIX B: SENSITIVITY OF RDE CHAMBER SIZE

The perimeter of RDE chamber is an important factor for RDW propagation because it determines the period of RDW and further influences the RDW height when the reactant and injection conditions keep fixed. In liquid-fuel RDEs, the droplet dynamics, residence time in the refill zone and vaporization timescale, may also be affected by the chamber perimeter. Figures 16(a) and 16(b) show the contours of gas temperature overlaid by Lagrangian droplets with the azimuthal lengths $L = 153$ and 306 mm, respectively. The former has been used in this study. The RDW height in Fig. 16(a) is obviously lower than that in Fig. 16(b), because of the longer period for RDW propagation when $L = 306$ mm. The longer injection time leads to longer residence time for the droplets in the refill zone, so more *n*-heptane burns on the deflagration surface and the deflagration combustion is stronger in Fig. 16(b) than that in Fig. 16(a). Despite the above differences, the flow structure and droplet distribution in the chamber are similar. As such, this comparison indicates that the azimuthal length used in the current study ($L = 153$ mm) is reasonable and can ensure the key features in two-phase rotating detonations are captured.

APPENDIX C: GRID SENSITIVITY ANALYSIS

Grid sensitivity in two-phase RDE simulations is analyzed with three resolutions, i.e., 25, 50, and $100\ \mu\text{m}$. They are termed as M1, M2, and M3, respectively. Table III summarizes the detonation propagation speeds predicted with three mesh resolutions. The detonation speed slightly increases as the grid size reduces, and the deviations from Chapman – Jouguet detonation speed are small for all the three cases. The stability of instantaneous detonation speed can be measured by standard deviation, i.e., s . This is calculated based on the time series of detonation propagation speed over about 10 cycles. According to Table III, more speed fluctuations can be captured (high s) as the mesh resolution decreases.

Figure 17 shows the droplet mean diameter (d_{10}) variations along the RDE height with the foregoing meshes. The droplet mean diameter in M3 is generally larger than those in M1 and M2. The

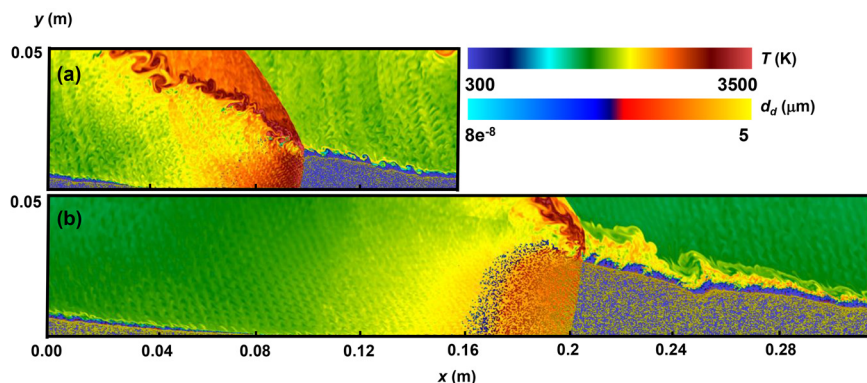


FIG. 16. Contours of gas temperature overlaid by Lagrangian fuel droplets: (a) $L = 153$ mm; (b) $L = 306$ mm. The prevaporized gas temperature and equivalence ratio are 400 K and 0.8, respectively.

TABLE III. RDW propagation speeds predicted with different meshes.

Mesh	Δ (μm)	D_{det} (m/s)	D_{CJ} (m/s)	Deficit (C–J, %)	Deviation (M1, %)	s
M1	25	1805	1829	1.3	—	343
M2	50	1796		1.8	0.5	320
M3	100	1786		2.4	1.1	256

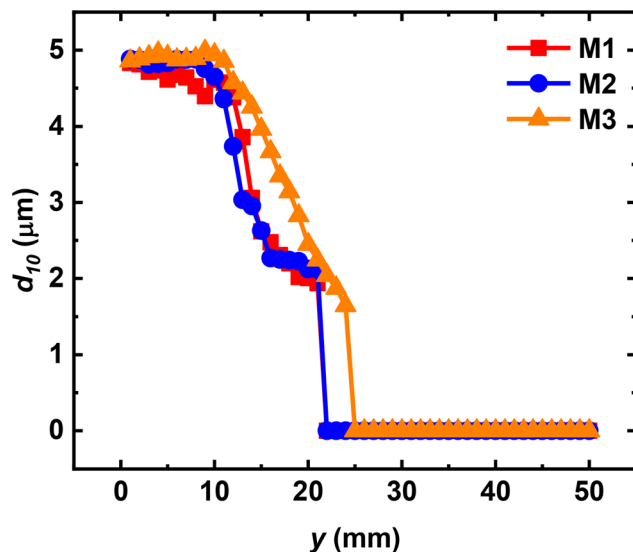


FIG. 17. Comparisons of mean droplet diameter variations along the RDE height.

latter two have similar profiles of mean droplet diameters along the RDE height direction, which indicates that the droplet evaporation in the rotating detonation flow field is correctly predicted. Based on Table III and Fig. 17, the mesh resolution of $50\text{ }\mu\text{m}$ is selected, as a compromise between computational accuracy and cost.

APPENDIX D: DETONATION CELL SIZE

Detonation cell sizes of pure gas cases with the same gas temperature (400 K) and different prevaporized degrees are shown in

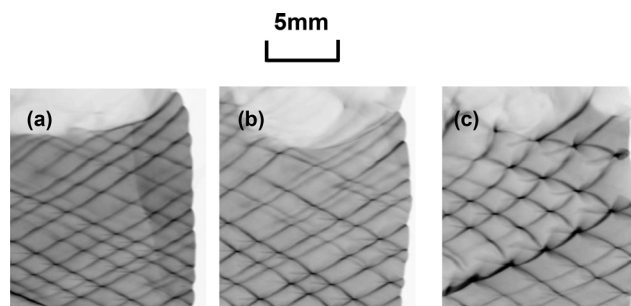
FIG. 18. Trajectories of peak pressure: (a) $T=400\text{ K}$, $\phi_g=0.8$; (b) $T=400\text{ K}$, $\phi_g=0.7$; (c) $T=400\text{ K}$, $\phi_g=0.65$; Image size is $0.0132\text{ m} \times 0.0136\text{ m}$.

Fig. 18. It can be found that the detonation cell size becomes regular and small as the prevaporized gas equivalence ratio increases from 0.65 to 0.8. Figures 18(a)–18(c) correspond to their two-phase cases of Figs. 14(b), 14(d), and 14(e). When ϕ_g is 0.7 or 0.8, the detonation cell size seems more regular in two-phase cases [Figs. 14(b) and 14(d)] than that in pure gas cases [Figs. 18(a) and 18(b)]. This indicates that the addition of *n*-heptane sprays enhances the stability of RDW. For $\phi_g=0.65$, the cell size is more regular in pure gas case than that in two-phase case as shown in Figs. 14(e) and Fig. 18(c). This may be because more droplets evaporate behind the RDW when the prevaporization degree is lowered, and these unburned droplets further influence the transverse wave propagation.

DATA AVAILABILITY

The data that support the findings of this study are available from the corresponding author upon reasonable request.

REFERENCES

- V. Anand and E. Gutmark, "Rotating detonation combustors and their similarities to rocket instabilities," *Prog. Energy Combust. Sci.* **73**, 182–234 (2019).
- P. Wolański, "Detonative propulsion," *Proc. Combust. Inst.* **34**, 125–158 (2013).
- J. Koch and J. N. Kutz, "Modeling thermodynamic trends of rotating detonation engines," *Phys. Fluids* **32**, 126102 (2020).
- L. Yan, Z. Weijiang, Y. Yunjun, L. Zhou, and W. Jianping, "Numerical study on the instabilities in H₂-air rotating detonation engines," *Phys. Fluids* **30**, 046106 (2018).
- P. Debnath and K. M. Pandey, "Numerical investigation of detonation combustion wave in pulse detonation combustor with ejector," *J. Appl. Fluid Mech.* **10**, 725–733 (2017).
- J. Li, W. Fan, W. Chen, K. Wang, and C. Yan, "Propulsive performance of a liquid kerosene/oxygen pulse detonation rocket engine," *Exp. Therm. Fluid Sci.* **35**, 265–271 (2011).
- Y. Fang, Y. Zhang, X. Deng, and H. Teng, "Structure of wedge-induced oblique detonation in acetylene-oxygen-argon mixtures," *Phys. Fluids* **31**, 026108 (2019).
- P. Yang, H. D. Ng, H. Teng, and Z. Jiang, "Initiation structure of oblique detonation waves behind conical shocks," *Phys. Fluids* **29**, 086104 (2017).
- A. Kawasaki, T. Inakawa, J. Kasahara, K. Goto, K. Matsuoka, A. Matsuo, and I. Funaki, "Critical condition of inner cylinder radius for sustaining rotating detonation waves in rotating detonation engine thruster," *Proc. Combust. Inst.* **37**, 3461–3469 (2019).
- Y. Zheng, C. Wang, Y. Wang, Y. Liu, and Z. Yan, "Numerical research of rotating detonation initiation processes with different injection patterns," *Int. J. Hydrogen Energy* **44**, 15536–15552 (2019).
- T. H. Yi, J. Lou, C. Turangan, J. Y. Choi, and P. Wolanski, "Propulsive performance of a continuously rotating detonation engine," *J. Propul. Power* **27**, 171–181 (2011).
- R. Zhou, D. Wu, and J. Wang, "Progress of continuously rotating detonation engines," *Chin. J. Aeronaut.* **29**, 15–29 (2016).
- J. Z. Ma, M. Luan, Z. Xia, J. Wang, S. Zhang, S. Yao, and B. Wang, "Recent progress, development trends, and consideration of continuous detonation engines," *AIAA J.* **58**, 4976–5035 (2020).

- ¹⁴P. Shen and T. Adamson, Jr., "Theoretical analysis of a rotating two-phase detonation in liquid rocket motors," NASA CR 122294 (1973).
- ¹⁵F. A. Bykovskii, S. A. Zhdan, and E. F. Vedernikov, "Continuous spin detonation of fuel-air mixtures," *Combust. Explos. Shock Waves* **42**, 463–471 (2006).
- ¹⁶F. A. Bykovskii, S. A. Zhdan, and E. F. Vedernikov, "Continuous spin detonation," *J. Propuls. Power* **22**, 1204–1216 (2006).
- ¹⁷F. A. Bykovskii, S. A. Zhdan, and E. F. Vedernikov, "Continuous spin detonation of a heterogeneous kerosene–air mixture with addition of hydrogen," *Combust. Explos. Shock Waves* **52**, 371–373 (2016).
- ¹⁸F. A. Bykovskii, S. A. Zhdan, and E. F. Vedernikov, "Continuous detonation of the liquid kerosene–air mixture with addition of hydrogen or syngas," *Combust. Explos. Shock Waves* **55**, 589–598 (2019).
- ¹⁹J. Kindracki, "Experimental studies of kerosene injection into a model of a detonation chamber," *J. Power Technol.* **92**, 80–89 (2012); available at <https://papers.itsc.pw.edu.pl/index.php/JPT/article/view/305>
- ²⁰J. Kindracki, "Experimental research on rotating detonation in liquid fuel–gaseous air mixtures," *Aerosp. Sci. Technol.* **43**, 445–453 (2015).
- ²¹B. Sun and H. Ma, "Two-dimensional numerical study of two-phase rotating detonation wave with different injections," *AIP Adv.* **9**, 115307 (2019).
- ²²A. K. Hayashi, N. Tsuboi, and E. Dzieminska, "Numerical study on JP-10/air detonation and rotating detonation engine," *AIAA J.* **58**, 5078–5094 (2020).
- ²³Q. Meng, M. Zhao, H. Zheng, and H. Zhang, "Eulerian-Lagrangian modelling of rotating detonative combustion in partially pre-vaporized n-heptane sprays with hydrogen addition," *Fuel* **290**, 119808 (2021).
- ²⁴C. T. Crowe, J. D. Schwarzkopf, M. Sommerfeld, and Y. Tsuji, *Multiphase Flows with Droplets and Particles* (CRC Press, 2011).
- ²⁵G. B. Macpherson, N. Nordin, and H. G. Weller, "Particle tracking in unstructured, arbitrary polyhedral meshes for use in CFD and molecular dynamics," *Commun. Numer. Methods Eng.* **25**, 263–273 (2009).
- ²⁶Z. Huang, M. Zhao, Y. Xu, G. Li, and H. Zhang, "Eulerian-Lagrangian modelling of detonative combustion in two-phase gas-droplet mixtures with OpenFOAM: Validations and verifications," *Fuel* **286**, 119402 (2021).
- ²⁷H. Zhang, see <http://blog.nus.edu.sg/huangwei/nus-ryrhocentralfoam-solver/> "National University of Singapore, Mechanical Engineering"
- ²⁸H. G. Weller, G. Tabor, H. Jasak, and C. Fureby, "A tensorial approach to computational continuum mechanics using object-oriented techniques," *Comput. Phys.* **12**, 620–631 (1998).
- ²⁹M. Zhao, J. Li, C. J. Teo, B. C. Khoo, and H. Zhang, "Effects of variable total pressures on instability and extinction of rotating detonation combustion," *Flow Turbul. Combust.* **104**, 261–290 (2020).
- ³⁰M. Zhao and H. Zhang, "Origin and chaotic propagation of multiple rotating detonation waves in hydrogen/air mixtures," *Fuel* **275**, 117986 (2020).
- ³¹C. J. Greenshields, H. G. Weller, L. Gasparini, and J. M. Reese, "Implementation of semi-discrete, non-staggered central schemes in a colocated, polyhedral, finite volume framework, for high-speed viscous flows," *Int. J. Numer. Methods Fluids* **63**, 1–21 (2009).
- ³²M. Zhao, M. J. Cleary, and H. Zhang, "Combustion mode and wave multiplicity in rotating detonative combustion with separate reactant injection," *Combust. Flame* **225**, 291–304 (2021).
- ³³A. Kurganov, S. Noelle, and G. Petrova, "Semidiscrete central-upwind schemes for hyperbolic conservation laws and Hamilton–Jacobi equations," *SIAM J. Sci. Comput.* **23**, 707–740 (2001).
- ³⁴C. K. Westbrook and F. L. Dryer, "Simplified reaction mechanisms for the oxidation of hydrocarbon fuels in flames," *Combust. Sci. Technol.* **27**, 31–43 (1981).
- ³⁵B. Franzelli, E. Riber, M. Sanjosé, and T. Poinso, "A two-step chemical scheme for kerosene–air premixed flames," *Combust. Flame* **157**, 1364–1373 (2010).
- ³⁶S. Liu, J. C. Hewson, J. H. Chen, and H. Pitsch, "Effects of strain rate on high-pressure nonpremixed n-heptane autoignition in counterflow," *Combust. Flame* **137**, 320–339 (2004).
- ³⁷J. Shepherd, see <https://shepherd.caltech.edu/edl/publicresources/sdt/> for "California Institute of Technology"
- ³⁸Y. Mahmoudi, K. Mazaheri, and S. Parvar, "Hydrodynamic instabilities and transverse waves in propagation mechanism of gaseous detonations," *Acta Astronaut.* **91**, 263–282 (2013).
- ³⁹S. Yao and J. Wang, "Multiple ignitions and the stability of rotating detonation waves," *Appl. Therm. Eng.* **108**, 927–936 (2016).
- ⁴⁰S. Yao, M. Liu, and J. Wang, "Numerical investigation of spontaneous formation of multiple detonation wave fronts in rotating detonation engine," *Combust. Sci. Technol.* **187**, 1867–1878 (2015).
- ⁴¹D. Schwer and K. Kailasanath, "Numerical investigation of the physics of rotating detonation engines," *Proc. Combust. Inst.* **33**, 2195–2202 (2011).
- ⁴²N. Tsuboi, Y. Watanabe, T. Kojima, and A. K. Hayashi, "Numerical estimation of the thrust performance on a rotating detonation engine for a hydrogen-oxygen mixture," *Proc. Combust. Inst.* **35**, 2005–2013 (2015).
- ⁴³J. Li, P. Chang, L. Li, Y. Yang, C. Teo, and B. Khoo, "Investigation of injection strategy for liquid-fuel rotating detonation engine," AIAA Aerospace Sciences Meeting, Kissimmee, Florida (2018).
- ⁴⁴R. W. Houim and R. T. Fievisohn, "The influence of acoustic impedance on gaseous layered detonations bounded by an inert gas," *Combust. Flame* **179**, 185–198 (2017).
- ⁴⁵P. Dai, C. Qi, and Z. Chen, "Effects of initial temperature on autoignition and detonation development in dimethyl ether/air mixtures with temperature gradient," *Proc. Combust. Inst.* **36**, 3643–3650 (2017).
- ⁴⁶C. K. Law, *Combustion Physics* (Cambridge University Press, 2006).
- ⁴⁷Y. Zhuang, Q. Li, P. Dai, and H. Zhang, "Autoignition and detonation characteristics of n-heptane/air mixture with water droplets," *Fuel* **266**, 117077 (2020).
- ⁴⁸M. Lesieur, O. Metais, and P. Comte, *Large-Eddy Simulation of Turbulence* (Cambridge University Press, 2005).
- ⁴⁹V. Duke-Walker, W. Maxon, S. Almuha, and J. McFarland, "Evaporation and breakup effects in the shock-driven multiphase instability," *J. Fluid Mech.* **908**, A13 (2021).
- ⁵⁰Z. Huang and H. Zhang, "On the interactions between a propagating shock wave and evaporating water droplets," eprint [arXiv:2011.02071](https://arxiv.org/abs/2011.02071) (2020).
- ⁵¹G. Gai, O. Thomine, S. Kudriakov, and A. Hadjadj, "A new formulation of a spray dispersion model for particle/droplet-laden flows subjected to shock waves," *J. Fluid Mech.* **905**, A24 (2020).